High-speed dual-view photoacoustic imaging pen

Wuyu Zhang,[1,2] Haigang Ma,[1,2] Zhongwen Cheng,[1,2] Zhiyang Wang,[1,2] Kedi Xiong,[1,2] and Sihua Yang[1,2,*]

[1]*MOE Key Laboratory of Laser Life Science and Institute of Laser Life Science, South China Normal University, Guangzhou 510631, China*
[2]*Guangdong Provincial Key Laboratory of Laser Life Science, College of Biophotonics, South China Normal University, Guangzhou 510631, China*
Corresponding author: yangsh@scnu.edu.cn

Today, photoacoustic imaging (PAI) is widely used to study diseases in the skin, brain, cardiovascular, and other parts. However, these studies are often carried out using physiological slices or model animals, which indicate that many PAI techniques can only be used in the laboratory. In order to promote the transformation of PAI into clinical applications or, more specifically, to extend the application of photoacoustic (PA) microscopy to areas such as the oral cavity, throat, cervix, and abdominal viscera which are difficult to detect with conventional PA microscopy systems, a PAI pen was developed. The PAI pen can be handheld and can perform forward detection and lateral detection. The imaging area is a 2.4 mm diameter circular area. In addition, it can provide a high-speed imaging mode of four frames per second and a high-resolution imaging mode of 0.25 frames per second to meet the different needs of clinical users. In this Letter, the performance of the PAI pen was tested by imaging the phantom and the human oral cavity. The experimental results prove that the PAI pen can clearly image the microvessels of the oral cavity, which indicates that it has the same imaging capability for other similar areas and has a good prospect for assisting the diagnosis of related diseases. © 2020 Optical Society of America

https://doi.org/10.1364/OL.388863

In the field of biomedical imaging, photoacoustic imaging (PAI) as a non-invasive mesoscopic imaging technique, combining the advantages of optical imaging and ultrasound imaging, has been widely studied by researchers around the world [1–3]. As known, conventional optical imaging is based on the reflection of light and, by focusing the light, high-resolution images can be obtained [4]. Ultrasound imaging is based on the difference in acoustic impedance of different biological tissues [5]. Due to the small attenuation of ultrasound by biological tissue, the imaging depth is deep. PAI is an imaging technique based on optical absorption excitation and acoustic detection, which means that it is easy to obtain deep-penetrating, high-resolution, high-specificity, and high-contrast images. After the target absorbs the pulsed light or the modulated light of a specific wavelength, the spatial distribution of the target in the imaging space can be obtained by detecting the generated photo-induced ultrasonic

waves [6–10]. Since hemoglobin naturally has a high absorption for the light with the wavelength of 532 nm, PAI can be used for imaging blood vessels in a label-free manner [11–13].

By focusing the excitation light, scanning the light focus, detecting the ultrasonic waves generated at each scanning point, and finally projecting point-by-point, high-resolution three-dimensional (3D) spatial distribution images of the absorber in the imaging space can be obtained [14–23]. This is the optical-resolution photoacoustic microscopy (OR-PAM) involved in this Letter. Currently, *in vivo* imaging of narrow areas such as the oral cavity, throat, cervix, and abdominal viscera (especially the latter three) is a blind spot for conventional OR-PAM. Conventional OR-PAM systems often use motors to drive the probe to raster scan [13–15], which makes it difficult to achieve *in vivo* imaging for those narrow areas. Photoacoustic (PA) endoscopy is suitable for imaging circular lumens such as the intestinal canal and the esophagus with rotary scanning, but not suitable for imaging those areas mentioned above. In short, to extend the application of OR-PAM to the narrow areas such as the oral cavity, throat, cervix, and abdominal viscera, a miniaturized raster-scanning PA microscopy probe that can penetrate deep into the human body is needed.

Recently, many novel OR-PAM systems have been developed. Hajireza *et al.* used fast scanning mirrors and an image guide with 30,000 fiber pixels to build a real-time handheld OR-PAM system [24]. Chen *et al.*, Lin *et al.*, and Park *et al.* built handheld OR-PAM systems with two-axis microelectromechanical system (MEMS) scanners [25–27]. The above systems were not specifically designed to detect narrow areas of the human body, so the feasibility of using them to perform *in vivo* imaging in areas such as throat, cervix, and abdominal viscera is low. Combined with the advantages of the above systems and inheriting our previous work [28–30], a PAI pen, which can be handheld and can perform dual-view detection (forward or lateral detection), was developed. To the best of our knowledge, this is the first time that a PA microscopy probe has been made into an imaging pen that is suitable for clinical examination of areas such as the oral cavity, throat, cervix, and abdominal viscera. In this Letter, it was applied to image the human oral cavity. During the experiments, a suitable imaging view (forward or lateral) was selected according to the target imaging areas. The experimental results prove that the PAI pen is able to clearly
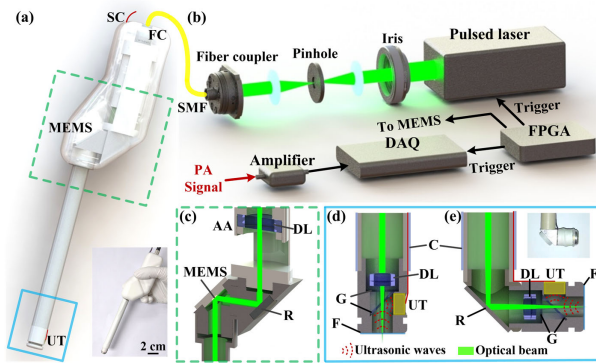
Fig. 1. Schematic of the system. (a) Schematic diagram of the PAI pen. (b) Composition of the PA system. (c) Enlarged cross-sectional view of the green dashed box in (a). (d)–(e) Enlarged cross-sectional views of the blue solid box in (a) when performing forward detection and lateral detection. FC, fiberport collimator; SC, signal cables; MEMS, microelectromechanical system scanner; SMF, single-mode fiber; DAQ, data acquisition; FPGA, field-programmable gate array; AA, axial adjuster; C, casing; DL, doublet lens; G, glass; UT, ultrasonic transducer; R, reflector; F, films.

image microvessels of the oral cavity, which indicates that it has the same imaging capability for other similar areas (such as throat, cervix, and abdominal viscera). This expands the clinical application of PA microscopy.

As shown in Fig. 1, the pulsed laser (Mosquitoo X 532-2-V, InnoLas) emits the 532 nm laser at a repetition rate of 50 kHz. The laser was spatially filtered and coupled by a fiberport coupler (PAF2-7 A, Thorlabs) to a single-mode fiber with a core diameter of 4 µm. After the light was collimated by a fiberport collimator (F240FC-532, Thorlabs), it was focused by a doublet lens (DLB-20-200PM, OptoSigma). The focused light was reflected 90 degrees by the reflector and then reflected by an FPGA-driven two-axis MEMS scanner (13Z2.1-3000, Mirrorcle Technologies Inc.) into another doublet lens (47-692-INK, Edmund). By changing the distance of the two doublet lenses, the axial position of the light focus can be adjusted. After the sample absorbed the pulsed laser, the generated ultrasonic waves were reflected by a 45 degree tilted glass sheet (thickness: 100 µm), and then detected by a cylindrical planar ultrasonic transducer (C10-4*3-1.5-SMA, Doppler Electronic Technologies Inc.) with the effective aperture of 4 mm and the center frequency of 10 MHz. During the experiments, water as the ultrasonic coupling medium was sealed in the ultrasonic detector by transparent films. When switching the forward detection mode to the lateral detection mode, a component with the 45 degree reflector needs to be added [as shown in Fig. 1(e)]. Additionally, the PA imaging resolution is the same. The final diameter of the distal head of the PAI pen is 12 mm.

Based on the premise that the target imaging areas of the PAI pen are areas such as the oral cavity, throat, cervix, and abdominal viscera, there are differences in the axial depth of blood vessels in different areas or different individuals. Therefore, a structure capable of adjusting the axial position of the light focus according to the actual clinical situation is needed. Considering the engineering difficulty and the compactness, a cylindrical axial adjuster (coaxial with the fiberport collimator) was designed, and the doublet lens was fixed in the axial adjuster. Through the screw thread, the axial position of the light focus

can be adjusted by rotating the axial adjuster. In addition, considering that in clinical applications the front end of the PAI pen needs to be in a narrow cavity, and it will inevitably come into touch with the human body, the axial adjuster is placed at the rear end of the PAI pen so that the pathogenic factors, which may be brought about when adjusting, can be prevented from touching the human body. However, this requires the use of a doublet lens with a long focal length, which means that the focusing ability is decreased, resulting in relatively poor lateral resolution of images. Therefore, a doublet lens with strong focusing ability is fixed at the front part of the PAI pen to decrease the size of the light spot and thereby improve the lateral resolution.

After the PA signals generated by the ultrasonic transducer were amplified by a 50 dB low noise amplifier (LNA-650, RFBAY), they were collected by a high-speed data acquisition card (M4i.4450-x8, Spectrum) at a sampling rate of 250 MHz and stored in a computer. The obtained PA signals were subjected to low-pass filtering with a cutoff frequency of 15 MHz, and then the wavelet transform was performed. The image reconstructions were performed by user-defined programs of LABVIEW (National Instruments) and MATLAB (R2016a, Math Works). The depth-encoded images were obtained by the functions provided by ImageJ (National Institutes of Health).

Since two doublet lenses were used to focus the light, the focus of the light was simulated using Zemax. The optical distance between the rear surface of the doublet lens (47-692-INK, Edmund) and the plane of the detection window is fixed to be 10 mm (2.5 mm in air and 10 mm in water). The simulation results when the distance between the rear surface of the doublet lens (DLB-20-200PM, OptoSigma) and the front surface of the doublet lens (47-692-INK, Edmund) is about 168 mm, and the light spot at the detection window is the smallest. As shown in Fig. 2(a), the energy distribution of the light focus was simulated under the above conditions. The resolutions of the PA system were characterized by imaging the sharp blade [as shown in Fig. 2(b)]. The distribution of the maximum amplitude of the PA signals corresponding to the dashed line was obtained. Then using the ORIGIN, these discrete values were fitted to obtain the edge spread function (ESF) curve. The line spread function curve, whose full width at half-maximum (FWHM) indicates the lateral resolution of the imaging system, was obtained by calculating the first derivative of the ESF curve. As can be seen from Fig. 2(c), the lateral resolution of the PA system is about 18.2 µm. By calculating the FWHM of a typical PA A-line signal (after Hilbert transform), as shown in Fig. 2(d), the axial resolution of the system was estimated to be 137.4 µm.

Due to the possible inconsistency of the lateral resolution at the center and the edge of the imaged area, the experiments shown in Figs. 2(e) and 2(f) were performed. The imaged samples are black grids with the line width of 30 µm and the pitch of 60 µm [as shown in Fig. 2(e)]. Figure 2(f) is a PA maximum amplitude projection (MAP) image of the samples. As can be seen from Fig. 2(f), the largest imaging field of the PAI pen is a circular area with a diameter of 2.4 mm. Additionally, in the imaging area, the difference in lateral resolution between the center and the edge does not affect the imaging result. It is observed that there are some slight distortions in PA images. The most likely cause is the unevenness of the two glass sheets at the front end, which causes different sizes of laser spots. In addition,
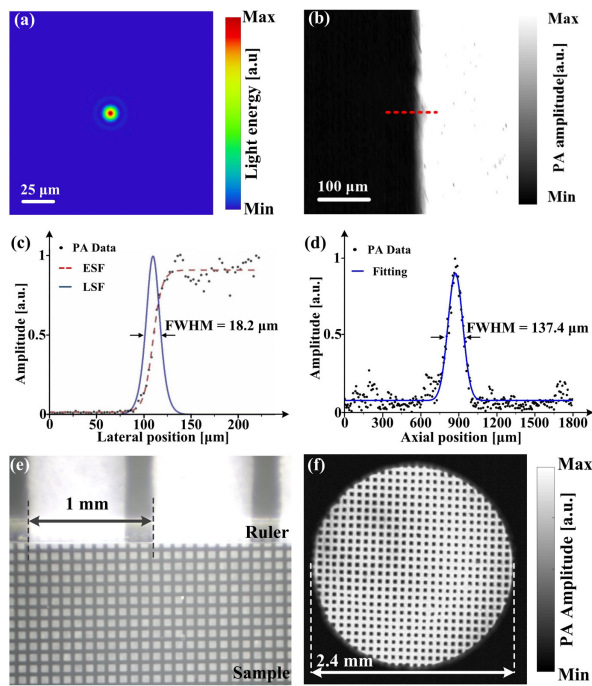
Fig. 2. Characterization of system performance. (a) Simulation of light focus. (b) PAI of the blade. (c) Lateral resolution of the system. (d) Axial resolution of the system. (e) Photograph of the sample. (f) Characterization of the size of the imaging area. (The speed of sound in the water was set to 1500 m/s.)

Fig. 3. Large field-of-view PA MAP image of blood vessels in the lower lip, which was reconstructed by stitching images obtained in the high-speed imaging mode [Visualization 1 (16 s)].

the unevenness of the water-sealed film may also affect the image quality slightly.

To assist clinicians in the diagnosis of diseases, two imaging modes are designed for clinical users: a high-speed imaging mode and high-resolution imaging mode. In the high-speed imaging mode, the imaging speed is four frames per second, but the lateral resolution of the image is relatively low due to the large scanning step size (about 30 μm). In a high-resolution imaging mode, it takes 4 s to obtain a 400×400 pixel PA image. For clinical detection, the clinicians can first move the imaging pen to detect the area of interest in a high-speed imaging mode. After finding a suspected lesion, they switch to the high-resolution imaging mode and perform a more accurate diagnosis based on the high-resolution image. The switch between the two imaging modes is achieved by modifying the FPGA program.

In order to verify the ability of the PAI pen to reveal microvessels, the oral cavity of an Asian male volunteer was imaged using it. During the experiments, the Asian male volunteer sat in a chair and wore goggles to avoid potential laser damage. The energy at the focus of a single laser pulse was about 80 nJ. Due to the scattering of light by the epidermis, the light intensity of the 532 nm laser in the tissue was within the safety limit of the American National Standards Institute (20 mJ/cm²) [31]. The consent was obtained from the volunteer, and all procedures were approved by South China Normal University.

Visualization 1 (16 s) and Visualization 2 (8 s) in the supplementary materials show the imaging results of microvessels on the lower lip in the high-speed imaging mode. The general distribution of blood vessels was displayed, while changes in blood vessel morphology (possibly due to blood flow) were observed. Besides, if needed, the large field-of-view PA image (as shown
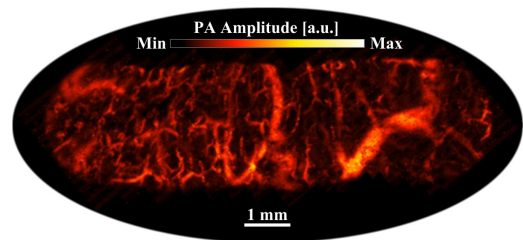
in Fig. 3) can be obtained by stitching the obtained PA images, which was achieved by a feature recognition algorithm [32].

Figure 4 shows the results of imaging different areas of the oral cavity in the high-resolution imaging mode. As shown in Figs. 4(a)–4(e), six representative areas of the oral cavity were imaged: the upper and lower lips, the sublingual, the left and right walls of the oral cavity, and the soft palate. The images of the upper and lower lips and the sublingual were obtained in the forward detection mode, and the images of the left and right walls of the oral cavity and the soft palate were obtained in the lateral detection mode. It can be observed that the small vessels in the superficial layer tend to grow axially, while the blood vessels in the deep layer are mainly submucosal drainage veins and arborescent vessels. This feature is particularly obvious at the lips and the soft palate, which is consistent with the characteristics of the blood vessels at the mucosa [33–35]. In addition, blood vessels in the sublingual were observed to be different in shape and depth from those in other areas. The reason should be that there are more glands in the sublingual, which leads to weaker light penetration [34]. Besides, Visualization 3 in the supplementary materials shows the layer-by-layer display of the result shown in Fig. 4(b). It is observed that there are some rod-like discontinuous vessels, which may due to the fact that, as the depth increased, the laser scattered, resulting in weak PA
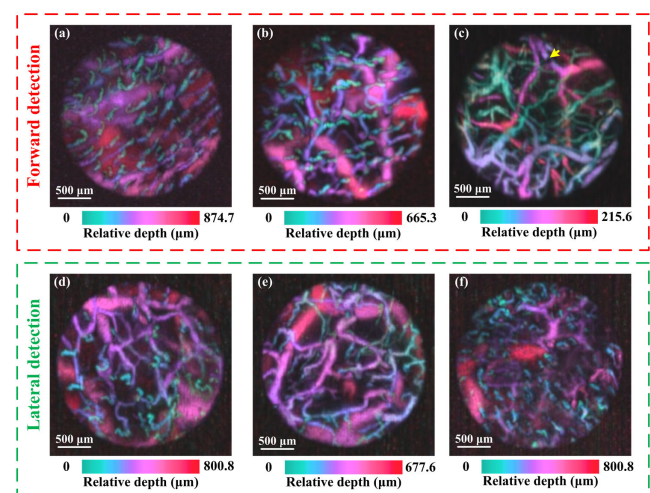

Fig. 4. PA depth-coded images of the microvessels in the oral cavity (obtained in the high-resolution imaging mode). (a) Upper lip (near the face), (b) lower lip (near the teeth), (c) sublingual, (d) left wall of the oral cavity, (e) right wall of the oral cavity, and (f) soft palate. The yellow arrow indicates a bubble. (The speed of sound in the tissue was set to 1540 m/s.)

signals, which will be drowning in background noise. Based on the above results, it is necessary to discuss the significance of the PAI pen in assisting the diagnosis of oral diseases. Oral cancer is life-threatening and has been widely studied by scientific researchers [34]. Most oral cancers are known to be squamous cell carcinomas. When early squamous cell carcinomas develop in the oral cavity, the microvessels of the lesion areas will have obvious morphological changes [33–35]. Thus, clear images of the microvessels from the oral mucosa and submucosa, which were obtained by the PAI pen, can assist to distinguish the conditions accurately.

To conclude, in this Letter, a PAI pen was developed. To the best of our knowledge, this is the first time that a PA microscopy probe being made into an imaging pen, which is suitable for clinical examination of areas such as the oral cavity, throat, cervix, and abdominal viscera. By imaging the human oral cavity, the PAI pen's ability to reveal microvessels was demonstrated. However, the PAI pen can be further improved. First, real-time imaging can be achieved if pulse lasers of higher repetition rate and faster scanners are available. Secondly, due to the light scattering by the deep tissue, the light energy is not enough to generate detectable ultrasound waves, making the current imaging depth limited. If a longer wavelength laser (such as 1064 nm) is used, the imaging depth will increase. Thirdly, if high sensitivity and clinically suitable wide-band ultrasound detectors are available, the axial resolution of images will be better, which is conducive to 3D image reconstructions. We will work on the above directions to perfect the PAI pen so that it can better assist clinicians in the diagnosis of related diseases. In addition, this Letter has proved that the PAI pen has a good prospect for imaging the throat, cervix, and abdominal viscera. Related research can be carried out later.

Disclosures. The authors declare no conflicts of interest.

REFERENCES

1. L. V. Wang and S. Hu, Science **335**, 1458 (2012).
2. M. Omar, J. Aguirre, and V. Ntziachristos, Nat. Biomed. Eng. **3**, 354 (2019).
3. P. Beard, Interface Focus **1**, 602 (2011).
4. R. K. Wang, S. L. Jacques, Z. Ma, S. Hurst, S. R. Hanson, and A. Gruber, Opt. Express **15**, 4083 (2007).
5. S. W. Smith, H. G. Pavy, and O. T. von Ramm, IEEE Trans. Ultrason. Ferr. **38**, 100 (1991).
6. C. Li, G. Ku, and L. V. Wang, Phys. Rev. E **78**, 021901 (2008).
7. J. Xia and L. V. Wang, IEEE Trans. Biomed. Eng. **61**, 1380 (2014).
8. S. Gottschalk, O. Degtyaruk, B. Mc Larney, J. Rebling, M. A. Hutter, X. L. Deán-Ben, S. Shoham, and D. Razansky, Nat. Biomed. Eng. **3**, 392 (2019).
9. W. Huang, R. Chen, Y. Peng, F. Duan, Y. Huang, W. Guo, X. Chen, and L. Nie, ACS Nano **13**, 9561 (2019).
10. W. Li, R. Chen, J. Lv, H. Wang, Y. Liu, Y. Peng, Z. Qian, G. Fu, and L. Nie, Adv. Sci. **5**, 1700277 (2018).
11. H. F. Zhang, K. Maslov, G. Stoica, and L. V. Wang, Nat. Biotechnol. **24**, 848 (2006).
12. Z. Yuan and H. Jiang, Appl. Phys. Lett. **88**, 231101 (2006).
13. Z. Chen, S. Yang, and D. Xing, Opt. Lett. **37**, 3414 (2012).
14. T. T. W. Wong, R. Zhang, C. Zhang, H. Hsu, K. I. Maslov, L. Wang, J. Shi, R. Chen, K. K. Shung, Q. Zhou, and L. V. Wang, Nat. Commun. **8**, 1386 (2017).
15. L. Wang, K. Maslov, J. Yao, B. Rao, and L. V. Wang, Opt. Lett. **36**, 139 (2011).
16. T. Jin, H. Guo, H. Jiang, B. Ke, and L. Xi, Opt. Lett. **42**, 4434 (2017).
17. B. Lan, W. Liu, Y. Wang, J. Shi, Y. Li, S. Xu, H. Sheng, Q. Zhou, J. Zou, U. Hoffmann, W. Yang, and J. Yao, Biomed. Opt. Express **9**, 4689 (2018).
18. B. Jiang, X. Yang, and Q. Luo, Opt. Express **24**, 20167 (2016).
19. Z. Guo, G. Li, and S. L. Chen, J. Biophotonics **11**, e201800147 (2018).
20. J. Meng, L. V. Wang, D. Liang, and L. Song, Opt. Lett. **37**, 4573 (2012).
21. H. Zhou, N. Chen, H. Zhao, T. Yin, J. Zhang, W. Zheng, L. Song, C. Liu, and R. Zheng, Photoacoustics **15**, 100143 (2019).
22. B. Rao, X. Leng, Y. Zeng, Y. Lin, R. Chen, Q. Zhou, A. R. Hagemann, L. M. Kuroki, C. K. McCourt, D. G. Mutch, M. A. Powell, I. S. Hagemann, and Q. Zhu, Sci. Rep. **9**, 14306 (2019).
23. S. Liu, X. Feng, H. Jin, R. Zhang, Y. Luo, Z. Zheng, F. Gao, and Y. Zheng, IEEE Trans. Med. Imaging **38**, 2037 (2019).
24. P. Hajireza, W. Shi, and R. J. Zemp, Opt. Express **19**, 20097 (2011).
25. Q. Chen, H. Guo, T. Jin, W. Qi, H. Xie, and L. Xi, Opt. Lett. **43**, 1615 (2018).
26. L. Lin, P. Zhang, S. Xu, J. Shi, L. Li, J. Yao, L. Wang, J. Zou, and L. V. Wang, J. Biomed. Opt. **22**, 041002 (2016).
27. K. Park, J. Y. Kim, C. Lee, S. Jeon, G. Lim, and C. Kim, Sci. Rep. **7**, 13359 (2017).
28. D. Xu, S. Yang, Y. Wang, Y. Gu, and D. Xing, Biomed. Opt. Express **7**, 2095 (2016).
29. H. Ma, Z. Cheng, Z. Wang, Y. Gu, T. Zhang, H. Qiu, and S. Yang, Appl. Phys. Lett. **113**, 083704 (2018).
30. W. Zhang, H. Ma, Z. Cheng, Z. Wang, L. Zhang, and S. Yang, Quantum Imag. Med. Surg. **9**, 807 (2019).
31. Laser Institute of America, American National Standard for Safe Use of Lasers ANSI Z136.1 (2014).
32. J. W. Baik, J. Y. Baik, J. Y. Kim, S. Cho, S. Choi, J. Kim, and C. Kim, IEEE Trans. Med. Imaging (2019).
33. C. A. Squier and M. J. Kremer, JNCI Monogr. **2001**, 7 (2001).
34. B. W. Neville and T. A. Day, CA Cancer J. Clin. **52**, 195 (2002).
35. H. Inoue, Digest. Endosc. **13**, S40 (2001).